

Structure Design of Soft Magnetic Materials Using Electron-Beam-Based Additive Manufacturing

Jing Yang,* Zongwen Fu,* and Carolin Körner

Fe_{93.5}Si_{6.5} (wt%) soft magnetic materials in toroidal shape are additively manufactured by means of electron beam powder bed fusion (PBF-EB). Different hatching strategies are applied to realize specific patterns of molten material alternating with non-molten powder particles. The specimens produced using different hatching strategies show identical relative densities but various structural features resulting in different magnetic properties. The magnetic performance of the specimens is characterized by determining hysteresis loops (*B–H* curves), power losses, and maximum magnetic flux density at frequencies between 50 and 1000 Hz. At constant mass, the different structures induced by using various hatching strategies have a strong influence on the hysteresis losses. These losses can be significantly reduced by applying a targeted structure design. The modified specimens show superior magnetic properties at sub-kHz compared to some soft magnetic materials fabricated by means of conventional methods and laser powder bed fusion (PBF-L).

1. Introduction

Soft magnetic materials, which can be easily (de)magnetized owing to high permeability and low coercivity,^[1–3] play a crucial role in alternating current (AC) applications (e.g., power stations, power generators, electric motors, transformers, and converters).^[4–6] Because silicon steel shows outstanding soft magnetic properties as well as a relatively low price, it is widely

used in the abovementioned fields and accounts for a market share of ≈80%.^[4,5,7] However, power losses (including hysteresis losses, eddy current losses and anomalous losses/excess eddy current losses) remarkably reduce energy efficiency and increase expenses;^[3,8–10] i.e., for transformers, the decrease of 1.5% in energy efficiency results in the extra cost of \$12 billion per year.^[1,2]

In traditional industries, silicon steel is usually produced via various steps, e.g., rolling of Fe–Si sheets, coating with non-conductive layers and stacking the coated sheets.^[10–13] Based on these fabrication methods, researchers have already put forward several solutions in terms of layer thickness and chemical composition to minimize power losses. Fischer et al.^[10,14,15] demonstrated that decreasing the layer thickness of the conventionally fabricated

silicon steel sheets helps to reduce eddy current losses and thereby power losses. In addition, Hilzinger et al.^[8,10,16,17] claimed that compared to the widely used conventional Fe_{97.0}Si_{3.0} (wt%) showing an electrical resistivity of 0.48 μΩm, Fe_{93.5}Si_{6.5} (wt%) possesses a much higher electrical resistivity of 0.82 μΩ m⁻¹, which helps to minimize eddy current losses and thereby power losses. However, owing to its brittle nature, Fe_{93.5}Si_{6.5} (wt%) is hard to be processed using conventional fabrication methods.^[11–13] Recently, the macroscopic design of Fe_{93.5}Si_{6.5} (wt%) was successfully achieved through laser powder bed fusion (PBF-L) to produce specimens in toroidal shape containing internal and external slits that significantly enhanced the electrical resistance to reduce the eddy current losses.^[9] Thus, additive manufacturing of Fe_{93.5}Si_{6.5} (wt%), which allows for designing structural features and tailoring the magnetic properties, attracts growing research interest in the last few years.^[3,18] However, due to the low preheating temperature during PBF-L, the additively manufactured Fe_{93.5}Si_{6.5} (wt%) exhibited cracks deteriorating the mechanical and magnetic properties.^[9,19]

Compared to PBF-L, electron beam powder bed fusion (PBF-EB) is a relatively young powder-bed-based additive manufacturing technology but shows unique characteristics.^[18,20–23] High processing temperature during the PBF-EB process helps to reduce thermal stresses and to overcome the issue of crack formation in the specimens. Yang et al.^[3] have already demonstrated that dense Fe_{93.5}Si_{6.5} (wt%) free of cracks and with a relative density of up to 99.99% were processable using PBF-EB. In addition, it is considered that PBF-EB perfectly meets the requirement for fabricating brittle Fe_{93.5}Si_{6.5} (wt%) with complex geometries

J. Yang, Z. Fu, C. Körner
Joint Institute of Advanced Materials and Processes
Friedrich-Alexander University Erlangen-Nürnberg
Dr.-Mack-Strasse 77, 90762 Fürth, Germany
E-mail: jing.jy.yang@fau.de; zongwen.fu@fgk-keramik.de

J. Yang, Z. Fu, C. Körner
Department of Materials Science
Chair of Materials Science and Technology for Metals
Friedrich-Alexander University Erlangen-Nürnberg
Martensstrasse 5, 91058 Erlangen, Germany

Z. Fu
Research Institute for Glass and Ceramics
Heinrich-Meister-Straße 2, 56203 Höhr-Grenzhausen, Germany

 The ORCID identification number(s) for the author(s) of this article can be found under <https://doi.org/10.1002/adma.202300837>

© 2023 The Authors. Advanced Materials published by Wiley-VCH GmbH. This is an open access article under the terms of the Creative Commons Attribution License, which permits use, distribution and reproduction in any medium, provided the original work is properly cited.

DOI: 10.1002/adma.202300837

and good magnetic performance at different frequencies.^[19,20] Furthermore, compared to conventional fabrication methods (including rolling, machining, coating, stacking...), PBF-EB, as a controllable layer-by-layer process, shows a high potential to produce soft magnetic end-use products in a single-step.^[1,2,20]

In this study, toroidal Fe_{93.5}Si_{6.5} (wt%) specimens with tailored structural features were successfully produced by means of PBF-EB using different hatching strategies. The correlation between the structure and the resulting magnetic properties is discussed. Based on the analyses, a modified structure is identified and successfully realized to further improve magnetic performance.

2. Experimental Section

Gas-atomized pre-alloyed Fe_{93.5}Si_{6.5} (wt%) powder (CHANGSHA EASCHEM Co., LIMITED, China) with a purity of more than 99.9% and a particle size ranging between 48 and 75 μm (Master-sizer 3000, Malvern Panalytical, UK) was used for PBF-EB. The Fe_{93.5}Si_{6.5} (wt%) powder showed an oxygen content of less than 0.03 wt% according to the oxygen analysis based on the carrier gas hot extraction method (EMGA 620 W, HORIBA Ltd., Japan). Toroidal specimens (Figure 1a, height: 6.3 mm, outer/inner diameter: 16.0 mm/9.6 mm) were printed using PBF-EB.

PBF-EB is a layer-by-layer additive manufacturing technology, and four steps are included to produce one layer, i.e., (1) applying a powder layer using raking; (2) preheating to slightly sinter the raked powder layer with good mechanical and electrical stability; (3) selective melting using defined hatching strategy to attain the required geometry (contour melting is used before hatching to guarantee good surface roughness); and (4) lowering the platform to get prepared for the next layer.^[20] Among all these steps, selective melting based on specific hatching strategies determines the final structure. Thus, using an appropriate hatching strategy plays a vital role in the PBF-EB process. Commonly, snake-shaped hatching is the most widely used scan strategy for PBF-EB. Nevertheless, when printing toroidal Fe_{93.5}Si_{6.5} (wt%) specimens by means of the snake-shaped hatching, geometric distortions (i.e., elliptical shape) were observed.^[3]

In this work, a Freemelt ONE machine (Freemelt AB, Mölndal, Sweden), which is an open-source PBF-EB system and allows for freely defining scan strategies, was applied to produce toroidal Fe_{93.5}Si_{6.5} (wt%) specimens. Two hatching strategies were applied: i) radial hatching and ii) circle hatching. During the radial hatching (after preheating and contour melting), the electron beam scans along the black lines from the inner edge to the outer edge forming a radial pattern (Figure 1d, the red arrow showing the moving direction of the electron beam). The angle between the two neighboring lines is named as angle offset (θ). Similarly, in the case of the circle hatching (after preheating and contour melting), the electron beam runs along the black circles clockwise forming a circular pattern (Figure 1e, the purple arrow showing the moving direction of the electron beam). The distance between the two neighboring circles is defined as circle offset (d).

Currently, the most widely used soft magnetic materials commonly show a multilayer structure, i.e., thin iron silicon layers are separated by polymeric insulation coating layers to reduce eddy current losses.^[8,9] In order to imitate the structure of the soft magnetic materials being widely used in industries, a multilayer structure containing “one hatching layer + one powder layer” is

designed (Figure 1b, the layer thickness is set to 50 μm). The hatching layer is generated by preheating, contour melting and hatching. The hatching layer is the most crucial source of ferromagnetism, which determines the final magnetic performance. The loose powder layer (Figure 1c) is composed of slightly sintered powder particles derived by preheating and contour melting of the raked powder layer. The sintered powder layer works as the insulation layer between two neighboring hatching layers to reduce eddy current losses. To explore the influence of the hatching strategies on magnetic performance, different specimens were fabricated using radial hatching and circle hatching, respectively (Figure 1d,e). During radial hatching, the angle offset (θ) was set to 8° (Figure 1d). As for circle hatching, 0.8 mm was utilized as the circle offset (Figure 1e). Moreover, the detailed processing parameters for PBF-EB are shown as follows: the preheating temperature of the powder bed was set to ≈900 °C. A beam power of 100 W and a scan speed of 500 mm s⁻¹ were applied for contour melting as well as hatching. To verify the reproducibility, more than three specimens were fabricated using the same processing parameters.

After PBF-EB, toroidal Fe_{93.5}Si_{6.5} (wt%) specimens were taken out of the slightly sintered powder bed through sandblasting using Fe_{93.5}Si_{6.5} (wt%) powder particles as blasting abrasive, followed by which, surface roughness (R_a , according to DIN EN ISO 25178) of toroidal Fe_{93.5}Si_{6.5} (wt%) specimens was tested using a laser scanning microscope (Lext OLS 4000, Olympus Corporation, Japan). Post-annealing for the specimens was conducted at 1150 °C for 1 h under vacuum conditions with a heating/cooling rate of 300 °C h⁻¹. Then, all specimens were weighed, and the relative density was calculated by dividing the weight of the specimens by 6.1 g (the weight of the fully dense specimen with the same volume is 6.1 g). To examine magnetic properties, toroidal Fe_{93.5}Si_{6.5} (wt%) specimens coiled with copper wire (7 windings at primary and secondary side) were tested by means of B - H Analyzers SY-8219 (IWATSU Test Instruments Corporation, Japan). First, power losses (P) and coercivity (H_c) were measured under the maximum magnetic flux density (B_m) of 0.1 T at frequencies (f) of 50, 60, 100, 400, 700 and 1000 Hz. Second, maximum magnetic flux density (B_m) and relative permeability (μ_r) were tested using the maximum magnetic field intensity (H_m) of 500 A m⁻¹ at frequencies (f) of 50, 60, 100, 400, 700 and 1000 Hz. In this study, the amplitude permeability (μ_a) is used as the relative permeability (μ_r) which is calculated as follows:^[24,25]

$$\mu_a = \mu_r = \frac{B_m}{H_m \mu_0} \quad (1)$$

where μ_a , μ_r , B_m , H_m , and μ_0 denote amplitude permeability, relative permeability, maximum magnetic flux density, maximum magnetic field intensity and vacuum permeability (constant, 1.256×10^{-6} N A⁻²), respectively.

After magnetic tests, the specimens were cut parallel to the build direction, followed by grinding, polishing and etching to investigate the structures by means of an optical microscope (AXIO Imager M1m, Carl Zeiss Jena GmbH, Germany). Furthermore, X-ray diffraction (XRD, Bruker D8 Advance eco, Bruker AXS GmbH, Germany) was utilized to detect the phases and global texture within different specimens using a scanning rate of 0.05°

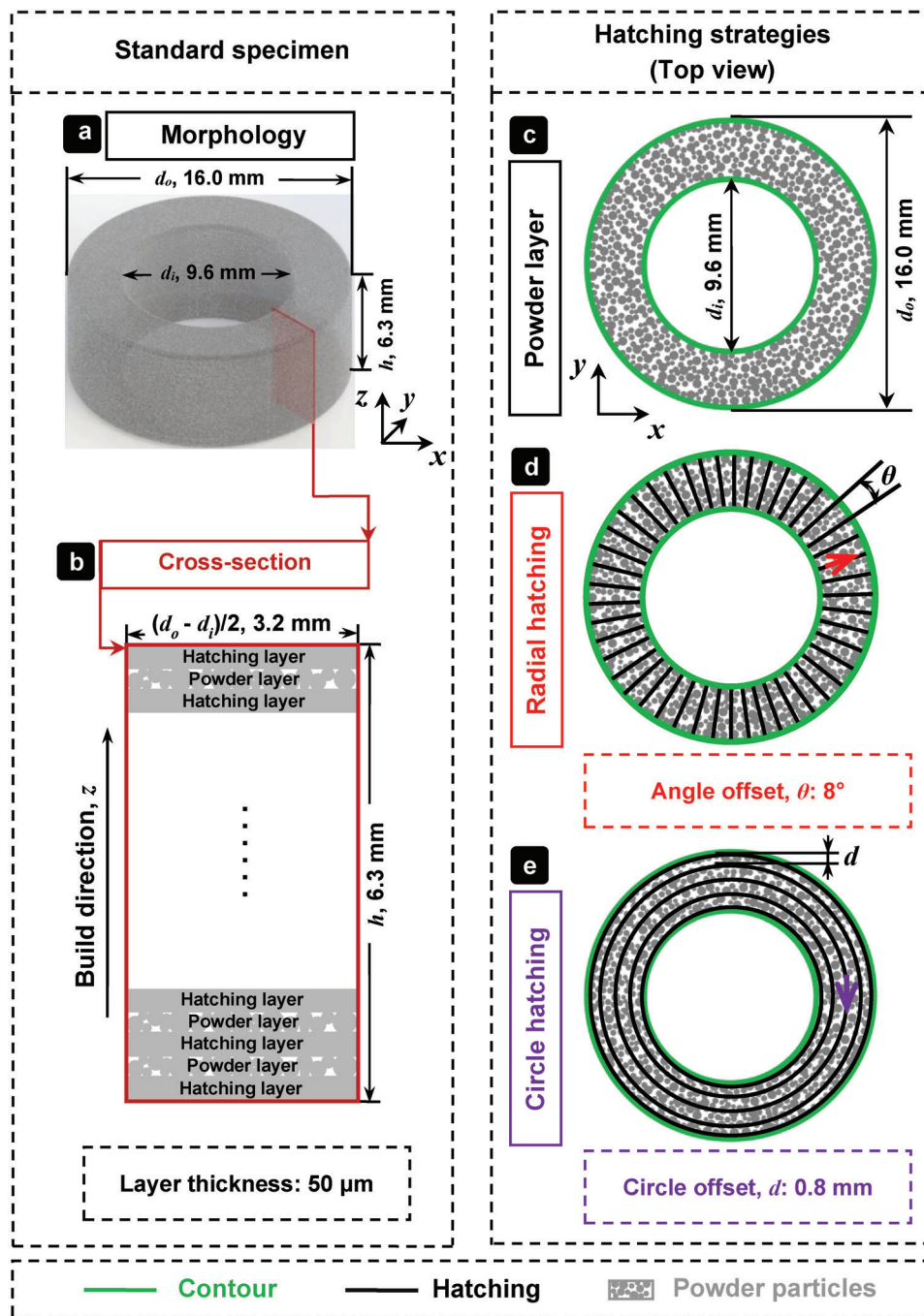


Figure 1. Hatching strategies designed for toroidal $\text{Fe}_{93.5}\text{Si}_{6.5}$ (wt%) specimens. a) Standard specimen shows a height (h) of 6.3 mm and an outer/inner diameter (d_o and d_i) of 16.0 mm/9.6 mm. The red square within the standard specimen represents the location of the cross-section shown in Figure 1b. b) A processing strategy based on “one hatching layer + one powder layer” was applied during PBF-EB. The layer thickness is set to 50 μm . The hatching layer stands for the ferromagnetic layer produced by means of preheating, contour melting and radial/circle hatching; while the powder layer is only preheated and contour-melted, which works as an insulation layer. c) The powder layer after preheating and contour melting is comprised of slightly sintered $\text{Fe}_{93.5}\text{Si}_{6.5}$ (wt%) powder particles. d) Radial hatching (the red arrow showing the moving direction of the electron beam) is in the control of angle offset (θ). In this study, the angle offset of 8° was used to produce radical-hatching specimens. e) Circle hatching (the purple arrow showing the moving direction of the electron beam) is determined by circle offset (d). In this study, the circle offset of 0.8 mm was utilized to fabricate circle-hatching specimens.

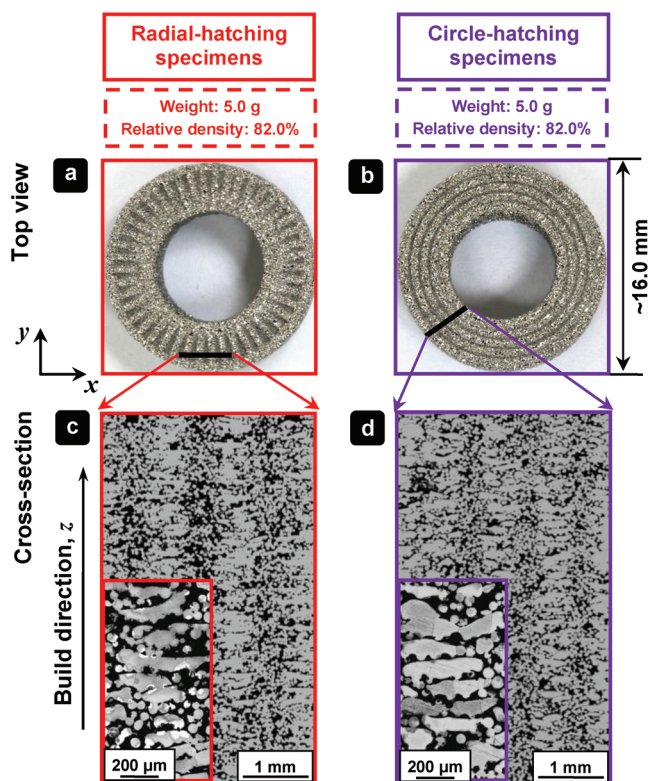


Figure 2. PBF-EB-produced toroidal $\text{Fe}_{93.5}\text{Si}_{6.5}$ (wt%) specimens fabricated by means of different hatching strategies using a beam power of 100 W and a scan speed of 500 mm s^{-1} . The radial-hatching specimens and circle-hatching specimens show the same weight of 5.0 g as well as the same relative density of 82.0%. a,b) Top views of the radial-hatching specimens and circle-hatching specimens. The black lines inserted in the top views indicate the location of the cross-sections shown in (c,d). c,d) Cross-sections of the radial-hatching specimens and circle-hatching specimens. Both specimens show a layered microstructure with an average layer thickness of $\approx 80 \mu\text{m}$ insulated by sintered $\text{Fe}_{93.5}\text{Si}_{6.5}$ (wt%) powder particles.

s^{-1} over a 2θ range of $30\text{--}90^\circ$, and a scanning electron microscope (SEM, Helios NanoLab600, FEI, America) equipped with an electron back-scattered diffraction (EBSD) detector was used to explore the local grain orientation.

3. Results and Discussion

The radial-hatching and circle-hatching specimens show different patterns from the top view (Figure 2a,b). In the cross-sections, which are parallel to the build direction and indicated by the black lines shown in Figure 2a,b, both specimens printed using various hatching strategies exhibit a similar layered microstructure with a comparable layer thickness of $\approx 80 \mu\text{m}$ (insets in Figure 2c,d). The molten layers resulting from hatching are insulated by the slightly sintered layers composed of loosely packed $\text{Fe}_{93.5}\text{Si}_{6.5}$ (wt%) powder particles. According to XRD and EBSD measurements, the radial-hatching specimens and the circle-hatching specimens exhibit a matrix of $\alpha\text{-Fe}$ (Si) solid solution and no significant grain orientation along the build direction (Figure S1 and S2 in supporting information).

Power losses and maximum magnetic flux density are the key factors affecting energy efficiency and power density. Power losses (P) are the sum of hysteresis losses (P_h), eddy current losses (P_e) and anomalous losses/excess eddy current losses (P_a), which can be expressed by Equation (2):^[1,3,8,19]

$$P = P_h + P_e + P_a \quad (2)$$

Hysteresis losses (P_h , calculated by Equation (3)) are caused by domain wall movement and domain rotation during (de)magnetization process, and it is represented by the area enclosed in the hysteresis loop.^{1,8,19}

$$P_h = k_h B_m^\alpha f \quad (3)$$

In Equation (3), k_h and α represent material constants, while B_m and f denote the maximum magnetic flux density and frequency. It has been demonstrated that decreasing impurities and increasing grain size as well as layer thickness help to reduce coercivity (H_c) and therefore hysteresis losses.^[1,3,8,19]

Eddy current losses (P_e) originate from the eddy current which follows the classical eddy current equation (Equation (4), valid for the materials with homogenous structure, no domains and constant permeability),^[8,26] and eddy current losses increase quadratically with the layer thickness. Thus, decreasing layer thickness can reduce eddy current losses significantly.^[1,3,8,19]

$$P_e = \frac{10^{-9} \pi^2 d^2 B_m^2 f^2}{6\rho} \quad (4)$$

In Equation (4), d , B_m , f , and ρ represent layer thickness, maximum magnetic flux density, frequency and electrical resistivity, respectively.

As for anomalous losses/excess eddy current losses (P_a), it is also caused by eddy current but does not fit with the classical eddy current equation due to defects and domain structures in the materials.^[1,3,8,19] Anomalous losses/excess eddy current losses can be calculated by Equation (5):

$$P_a = k_a B_m^\beta f^{1.5} \quad (5)$$

where k_a and β represent material constants, and B_m and f stand for maximum magnetic flux density and frequency.

In addition, maximum magnetic flux density (B_m)^[24,25] is proportional to the relative permeability (μ_r , see Equation (1)) of the material and the maximum magnetic field intensity (H_m) applied on the material, and it can be calculated by Equation (6):

$$B_m = \mu_0 \mu_r H_m \quad (6)$$

where B_m , μ_0 , μ_r , and H_m represent maximum magnetic flux density, vacuum permeability (constant, $1.256 \times 10^{-6} \text{ N A}^{-2}$), relative permeability and the maximum magnetic field intensity, respectively.

Figure 3 depicts the magnetic properties of radial-hatching specimens and circle-hatching specimens. Hysteresis loops (B – H curves) of the circle-hatching specimens are narrower than those of the radial-hatching specimens at 50 Hz (Figure 3a) as

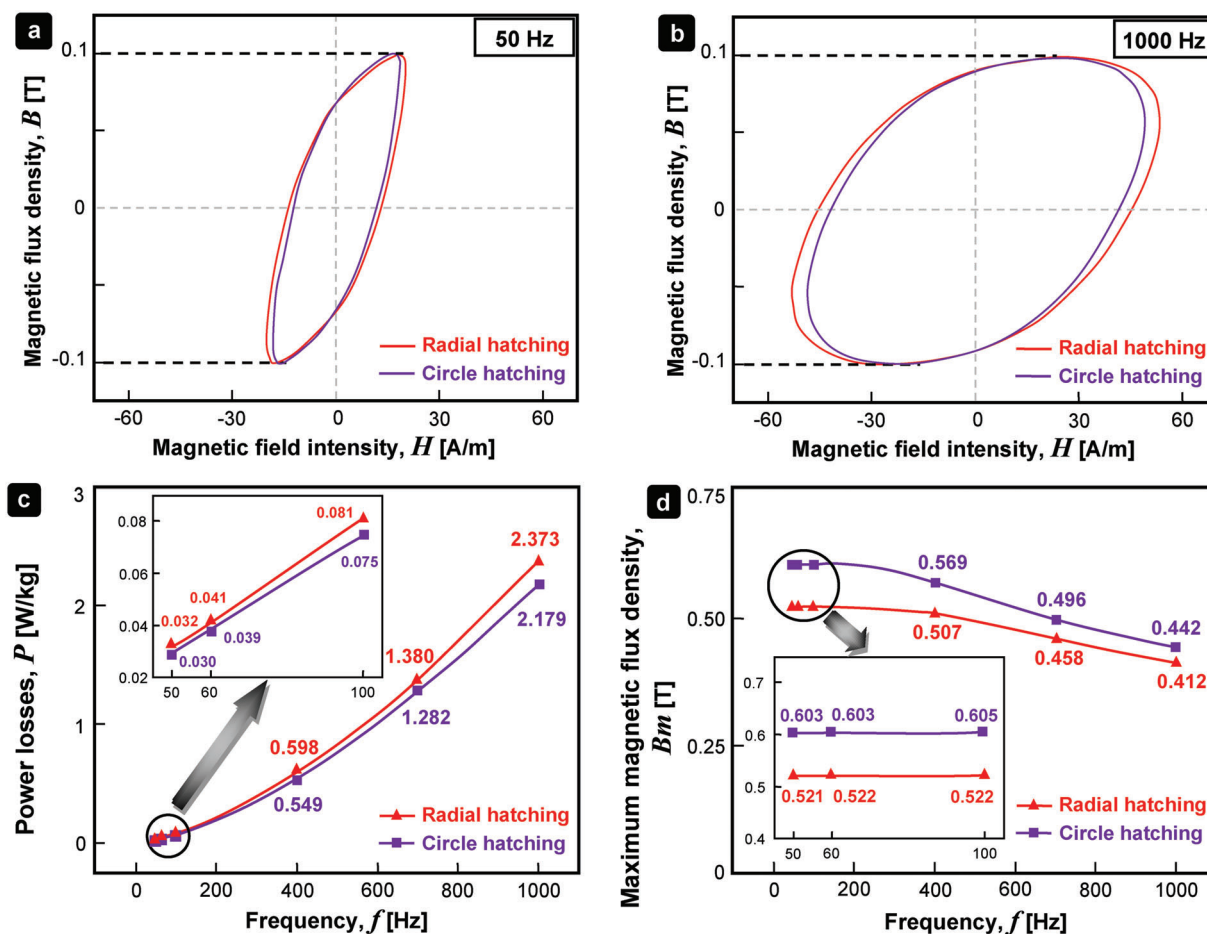


Figure 3. Magnetic properties of toroidal Fe_{93.5}Si_{6.5} (wt%) specimens fabricated using “radial hatching” and “circle hatching”. a,b) Hysteresis loops (B – H curves) of the radial-hatching specimens and circle-hatching specimens at frequencies of 50 Hz and 1000 Hz. The circle-hatching specimens show narrower hysteresis loops compared to those of the radial-hatching specimens, which qualitatively indicates that the circle-hatching specimens have lower hysteresis losses. c,d) The circle-hatching specimens show lower power losses and higher maximum magnetic flux density at various frequencies.

well as at 1000 Hz (Figure 3b). This indicates that the circle-hatching specimens have lower hysteresis losses (P_h , the area enclosed in the hysteresis loop^[19]).

To accurately quantify and compare the magnetic performance of the radial-hatching and circle-hatching specimens, power losses and maximum magnetic flux density at different frequencies are illustrated in Figure 3c,d. With the rise of the frequency, hysteresis losses increase. This is because the (de)magnetization process takes time and cannot follow the frequent change of the applied magnetic field at high frequencies, which leads to severe delay of (de)magnetization process.^[8] At the same time, the increase of the frequency also results in higher eddy current losses resulting from larger eddy current. Therefore, the power losses of the two specimens increase with the frequency (Figure 3c). However, the power losses of the circle-hatching specimens are lower than that of the radial-hatching specimens at all frequencies (Figure 3c), which can be explained by the aspects of hysteresis losses and eddy current losses. On the one hand, the circle-hatching specimens show a top view comprising concentric circles (Figure 2b), which coincide with the pathway of magnetic field lines (Figure 4a) and help to guide the magnetic flux, so

that the (de)magnetization process becomes easier.^[27–29] Therefore, the circle-hatching specimens show lower coercivity (H_c) (Table 1) and lower hysteresis losses (P_h , the area enclosed in the hysteresis loop in Figure 3a,b). On the other hand, the radial-hatching specimens and circle-hatching specimens display a similar microstructure with a comparable layer thickness of ≈ 80 μm (Figure 2c,d). Since eddy current losses are mainly affected by the thickness (Equation (4)), the two kinds of specimens should possess comparable eddy current losses. To summarize, the circle-hatching specimens have lower hysteresis losses but comparable eddy current losses compared to the radial-hatching specimens, so the circle-hatching specimens show smaller power losses.

In addition, the circle-hatching specimens show higher relative permeability (Table 1) and thereby higher maximum magnetic flux density (Equation (6)) than those of the radial-hatching specimens at different frequencies (Figure 3d). This can be explained from two aspects. First, the concentric circles shown in the top view of the circle-hatching specimens (Figure 2b) make the flow of magnetic flux easier. Second, the magnetization direction (Figure 4a) is parallel to the long dimension of the concentric circles in the circle-hatching specimens (Figure 2b),

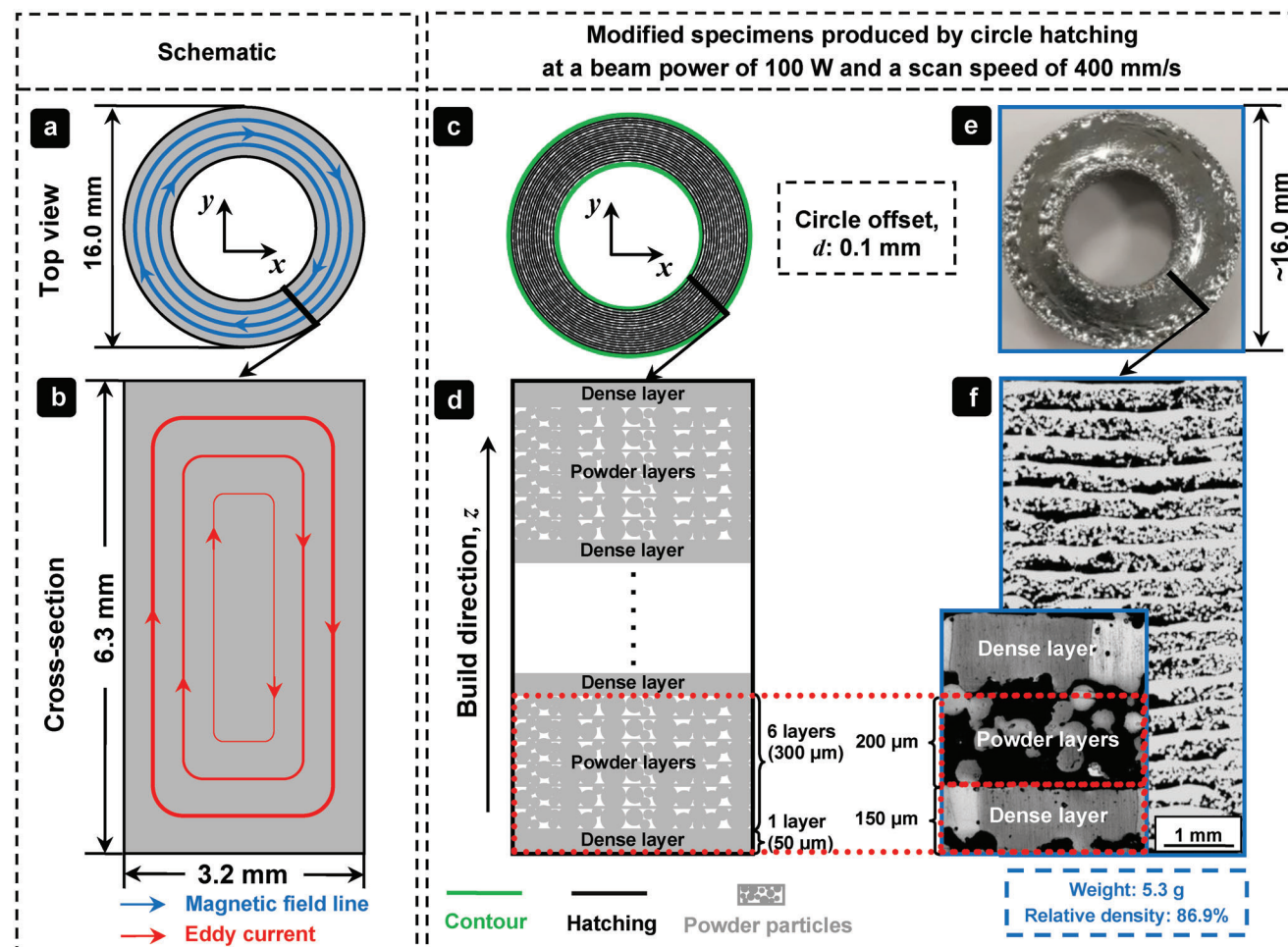


Figure 4. The modified $\text{Fe}_{93.5}\text{Si}_{6.5}$ (wt%) specimens with a specific structure of “one dense layer + powder layers” produced by means of PBF-EB based on the theory of electromagnetism. (The black lines inserted in the top views denote the location of the cross-sections.) a,b) Schematic showing the pathway of magnetic field lines and eddy current within a dense model based on the theory of electromagnetism. c,d) The design of the modified $\text{Fe}_{93.5}\text{Si}_{6.5}$ (wt%) specimens with the specific structural features printed using the following processing strategy: i) melting of a powder layer with a depth of 50 μm using circle-hatching; ii) 6 times raking and sintering of powder layers each with a thickness of 50 μm . e,f) Top view and microstructure of the modified $\text{Fe}_{93.5}\text{Si}_{6.5}$ (wt%) specimens produced using the abovementioned processing strategy. (Notes: The high porosity of the powder layers might be attributed to the mechanical preparation of the cross-section for the microstructure analysis; i.e., during grinding, the loosely packed particles in the slightly sintered powder layers could be peeled off and removed under the mechanical action.)

Table 1. Magnetic properties of toroidal $\text{Fe}_{93.5}\text{Si}_{6.5}$ (wt%) specimens fabricated using “radial hatching” and “circle hatching” during PBF-EB. P , H_c , B_m , and μ_r denote power losses, coercivity, maximum magnetic flux density and relative permeability, respectively. (Notes: To verify the reproducibility, several specimens fabricated using the same processing parameters were tested, and the deviation from the average value is shown below).

f [Hz]	Radial hatching				Circle hatching			
	P [W kg^{-1}]	H_c [A m^{-1}]	B_m [T]	μ_r	P [W kg^{-1}]	H_c [A m^{-1}]	B_m [T]	μ_r
50	0.032 ± 0.001	13.04 ± 0.10	0.521 ± 0.012	831 ± 20	0.030 ± 0.001	11.95 ± 0.08	0.603 ± 0.016	964 ± 27
60	0.041 ± 0.001	13.81 ± 0.11	0.522 ± 0.013	831 ± 20	0.039 ± 0.001	12.94 ± 0.12	0.603 ± 0.016	964 ± 23
100	0.081 ± 0.001	16.09 ± 0.08	0.522 ± 0.013	833 ± 18	0.075 ± 0.001	14.75 ± 0.09	0.605 ± 0.016	960 ± 22
400	0.598 ± 0.005	28.40 ± 0.23	0.507 ± 0.011	807 ± 17	0.549 ± 0.006	26.23 ± 0.18	0.569 ± 0.011	906 ± 15
700	1.380 ± 0.010	37.23 ± 0.65	0.458 ± 0.009	730 ± 12	1.282 ± 0.005	34.50 ± 0.36	0.496 ± 0.007	787 ± 12
1000	2.373 ± 0.003	44.59 ± 0.61	0.412 ± 0.008	654 ± 8	2.179 ± 0.001	41.11 ± 0.51	0.442 ± 0.006	704 ± 9

which leads to a smaller demagnetization field.^[8,26,30] While in the radial-hatching specimens, the magnetization direction (Figure 4a) is parallel to the short dimension of the molten lines in the radial pattern (Figure 2a), which results in a higher demagnetization field.^[8,26,30] It is also notable that the two kinds of specimens exhibit almost unchanged maximum magnetic flux density at the frequencies of 50, 60 and 100 Hz (the inset in Figure 3d) resulting from the near constant relative permeability (Table 1). However, the maximum magnetic flux density decreases slightly when increasing the frequency to 400 Hz or higher (Figure 3d). This is essentially caused by eddy current.^[1,31,32] At high frequencies, the eddy current gets larger due to higher electromotive force (the induced voltage), which cancels out the magnetic induction in the center according to Lenz's law and makes only the surface with a certain depth effective for magnetic induction,^[26] resulting in smaller relative permeability (Table 1) and therefore lower maximum magnetic flux density (Equation (6)). The cancellation of the magnetic induction in the center resulting from the eddy current is called the skin effect.^[1,26]

It is worth mentioning that, compared to the radial-hatching specimens, the power losses of the circle-hatching specimens were reduced by between $\approx 5\%$ (at low frequencies) and $\approx 9\%$ (at high frequencies), and the maximum magnetic flux density of the circle-hatching specimens was improved by at least 7% (Table S3 in supporting information). According to Ouyang et al.,^[1,2] for transformers, a decrease of 1.5% in energy efficiency results in extra costs of \$12 billion per year, worldwide. Therefore, the improvement in magnetic properties achieved in this work is promising.

In order to further improve the magnetic performance, the processing strategy based on the circle-hatching strategy was adapted. Simultaneously, new circle-hatching specimens (in the following called as "the modified specimens") with a specific structure were produced (Figure 4). The molten layers depicted in Figure 2 are discontinuous. Based on the state-of-the-art know-how, it is considered that a structure containing thin continuous dense layers separated by insulation layers could benefit the flow of magnetic flux (Figure 4a) and improve soft magnetic properties.^[19,26] Thus, circle-hatching with a circle offset of 0.1 mm (Figure 4c), a beam power of 100 W and a scan speed of 400 mm s⁻¹ were applied with the intention of achieving fully dense layers. Nevertheless, when using these circle-hatching parameters, the energy input for each layer significantly increases, resulting in a much higher melt pool depth and the vanishing of the porous insulation layers if only one powder layer is applied between two molten layers. Thus, after the circle-hatching of a raked powder layer with a layer thickness of 50 μm , six porous and slightly sintered powder layers (total thickness: 300 μm) were spread onto the molten layer to separate the two adjacent dense layers and interrupt the flow of eddy current (Figure 4b). This processing strategy is depicted in Figure 4d.

Figure 4e,f show the macroscopic top view and the microscopic cross-section of the modified Fe_{93.5}Si_{6.5} (wt%) specimens produced using the processing strategy shown in Figure 4c,d. According to the microstructure analysis (Figure 4f), the dense layers free of cracks show a thickness of $\approx 150 \mu\text{m}$ due to the higher energy input. At the same time, the slightly sintered powder layers exhibit a thickness of $\approx 200 \mu\text{m}$. Our previous study^[3] demonstrated that the dense Fe_{93.5}Si_{6.5} (wt%) alloy produced by means

of PBF-EB showed a high Vickers hardness of 366.7 HV30, which ensures good mechanical stability of the dense layers. As for the high porosity of the powder layers (Figure 4f), it might be attributed to the mechanical preparation of the cross-section for the microstructure analysis, i.e., during grinding, the loosely packed particles in the slightly sintered powder layers could be peeled off and removed under the mechanical action. Besides, the modified specimens show a matrix of $\alpha\text{-Fe}$ (Si) solid solution and no significant grain orientation along the build direction based on XRD and EBSD tests (Figure S1 and S2 in supporting information).

Compared to the results shown in Figure 3, the modified Fe_{93.5}Si_{6.5} (wt%) specimens produced using the specifically designed processing strategy show much narrower hysteresis loops (B - H curves) at frequencies of 50 Hz and 1000 Hz (Figure 5a,b) which indicate lower hysteresis losses. This can be explained by the fact that the dense layers with fewer defects embedded in the modified specimens allow for a significantly easier (de)magnetization process, leading to lower coercivity at different frequencies (Table 2). At the same time, the loosely packed powder particles inserted between the dense layers block the flow of the eddy current and increase the electrical resistance, which helps to reduce eddy current losses. Therefore, much lower power losses were determined for the modified specimens (Table 2). In addition, it is worth mentioning that the modified Fe_{93.5}Si_{6.5} (wt%) specimens display much higher maximum magnetic flux density at different frequencies (Table 2) compared to the results shown in Figure 3, which also results from the dense layers, providing a smoother pathway for the flow of magnetic flux and thereby a higher relative permeability (Table 2). However, with increasing frequency from 400 Hz, the maximum flux density of the modified specimens declines (Table 2), which can be explained by the skin effect^[1] as discussed above. In order to impede the skin effect and obtain higher maximum magnetic flux density at high frequencies, it is effective to decrease the layer thickness.^[31,32]

In addition, the magnetic properties of the modified specimens (Figure 5c) were compared with those of Fe_{93.5}Si_{6.5} (wt%) soft magnetic materials produced using conventional methods, including "powder core" (Figure 5d, fabricated by means of coating, bonding and cold pressing with ball-milled powder particles with a diameter of $\approx 100 \mu\text{m}$)^[8] and "flake core" (Figure 5e, produced through coating, bonding and cold pressing with melt-spun flakes with a thickness of $\approx 100 \mu\text{m}$).^[8]

As shown in Figure 5f, the "powder core" displays the highest power losses at all frequencies. The reason for this is that the polymeric insulation materials interrupt the flow of magnetic flux, and the spherical powder particles result in a large demagnetization factor of 0.333 and a large demagnetization field.^[8,30] These two factors make it difficult to (de)magnetize the "powder core" and lead to significant hysteresis losses, accounting for the major part of the power losses. This can be demonstrated by the linear fitting for $\log(P)$ - $\log(f)$ of the "powder core", which shows a relationship of " $P \propto f^{1.11}$ " between the power losses and the frequency (Figure 5g), similar to the relationship between the hysteresis losses and the frequency, namely " $P_h \propto f$ " (Equation (3)). As for the "flake core", the linear fitting for $\log(P)$ - $\log(f)$ displays a correlation of " $P \propto f^{1.12}$ " (Figure 5g), so hysteresis losses are also the main part of power losses. Because the specific

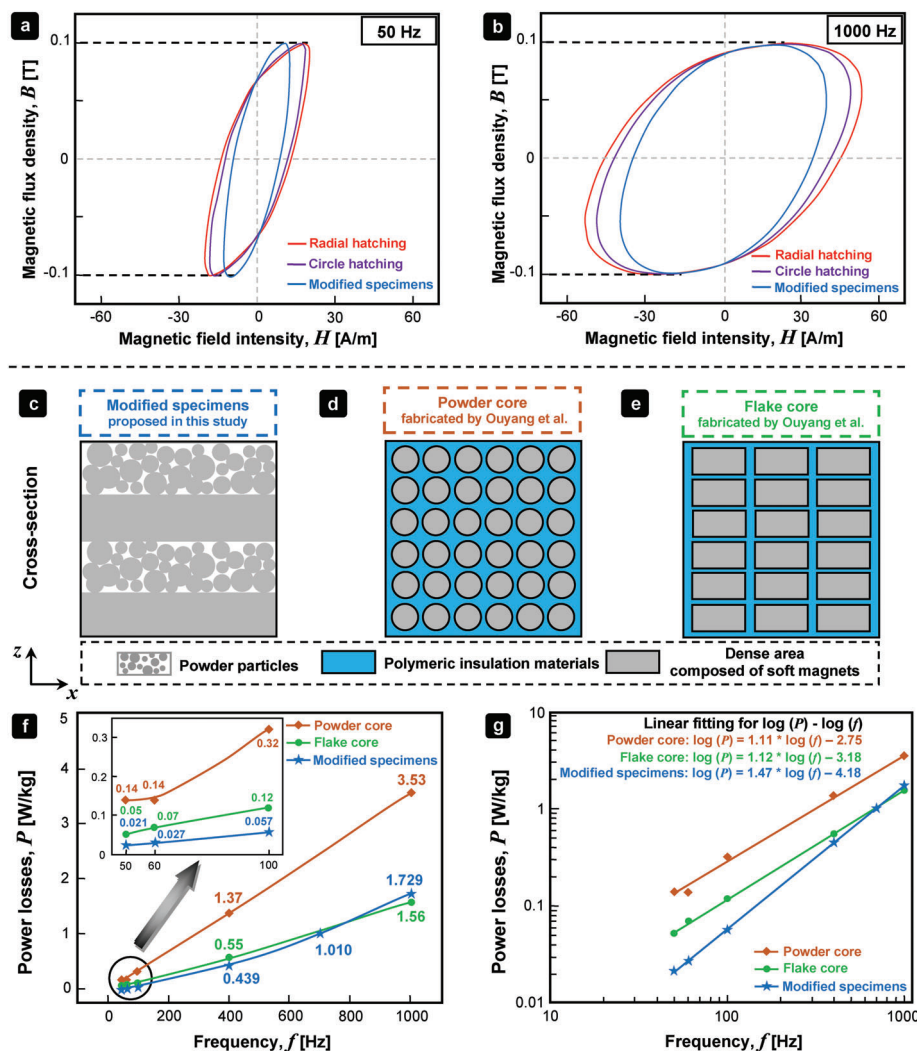


Figure 5. Magnetic properties of toroidal $\text{Fe}_{93.5}\text{Si}_{6.5}$ (wt%) specimens produced by means of PBF-EB and two reference specimens (“powder core” and “flake core”) with the same chemical composition fabricated by conventional methods.^[8] a, b) Hysteresis loops (B – H curves) of toroidal $\text{Fe}_{93.5}\text{Si}_{6.5}$ (wt%) specimens at the frequencies of 50 Hz and 1000 Hz. The modified specimens show much narrower hysteresis loops compared to those of radial-hatching and circle-hatching specimens as depicted in Figure 3, which qualitatively indicates that the modified specimens possess much lower hysteresis losses. c–e) Schematics showing the cross-sections of the modified specimens, “powder core” and “flake core”. The “powder core” consists of the coated powder particles with a diameter of $\approx 100 \mu\text{m}$ embedded in the polymeric insulation materials,^[8] and the “flake core” is comprised of the coated flakes with a thickness of $\approx 100 \mu\text{m}$ embedded in the polymeric insulation materials.^[8] f) The power losses of the modified specimens, “powder core”^[8] and “flake core”.^[8] g) Linear fitting for $\log(P)$ – $\log(f)$ of the modified specimens, “powder core”^[8] and “flake core”^[8] in log–log coordinate. (Notes: The linear fitting results shown in the figure possess a high COD (coefficient of determination) larger than 0.99, indicating high fitting accuracy.)

shape of the flakes helps to decrease the demagnetization factor to 0.0439 leading to a smaller demagnetization field and allows for large grain structure,^[8,30] the “flake core” shows lower hysteresis losses and thereby lower power losses compared to the “powder core”. As discussed before, the continuous dense molten layers reduce hysteresis losses dramatically, which is in control of the power losses at low frequencies, so the modified specimens exhibit the lowest power losses at low frequencies between 50 Hz and 400 Hz. However, the power losses of the modified specimens at 1000 Hz are slightly higher than that of the “flake core”. This is because the modified specimens have a higher layer thickness of $\approx 150 \mu\text{m}$ than that of the “flake core” ($\approx 100 \mu\text{m}$),^[8] which causes higher eddy current losses (Equation (4)) dominat-

ing the power losses at high frequency. This is consistent with the linear fitting for $\log(P)$ – $\log(f)$ of the modified specimens, indicating a relationship of “ $P \propto f^{1.47}$ ” (Figure 5g). Because hysteresis losses, eddy current losses and anomalous losses/excess eddy current losses are proportional to f (Equation (3)), f^2 (Equation (4)) and $f^{1.5}$ (Equation (5)), respectively, the relationship of “ $P \propto f^{1.47}$ ” demonstrates that the power losses of the modified specimens should consist of hysteresis losses, eddy current losses and anomalous losses/excess eddy current losses. To overcome the high eddy current losses at high frequency, a further reduction in the layer thickness of the PBF-EB-processed specimens by applying smaller powder particles would be a feasible solution.

Table 2. Magnetic properties of the modified Fe_{93.5}Si_{6.5} (wt%) specimens produced by means of PBF-EB and two reference specimens (“powder core” shown in Figure 5d and “flake core” illustrated in Figure 5e) with the same chemical composition fabricated by conventional methods.^[8] P , H_c , B_m , and μ_r denote power losses, coercivity, maximum magnetic flux density and relative permeability, respectively.

f [Hz]	Modified specimens ^{a)}				Reference specimens ^[8]	
	P [W kg ⁻¹]	H_c [A m ⁻¹]	B_m [T]	μ_r	Powder core P [W kg ⁻¹]	Flake core P [W kg ⁻¹]
50	0.021 ± 0.001	8.84 ± 0.03	0.902 ± 0.003	1441 ± 4	0.14	0.05
60	0.027 ± 0.001	9.44 ± 0.10	0.902 ± 0.003	1441 ± 9	0.14	0.07
100	0.057 ± 0.001	11.81 ± 0.14	0.900 ± 0.003	1438 ± 6	0.32	0.12
400	0.439 ± 0.003	22.30 ± 0.23	0.820 ± 0.001	1309 ± 4	1.37	0.55
700	1.010 ± 0.017	29.12 ± 0.41	0.663 ± 0.001	1059 ± 2	–	–
1000	1.729 ± 0.016	34.82 ± 0.38	0.569 ± 0.001	903 ± 1	3.53	1.56

^{a)} To verify the reproducibility, several modified specimens fabricated using the same processing parameters were tested, and the deviation from the average value is shown.

According to the results mentioned before, the modified specimens display the lowest power losses at frequencies between 50 Hz and 400 Hz, which proves that the modified specimens fabricated by means of PBF-EB outperform the conventionally produced “powder core”^[8] and “flake core”^[8] at sub-kHz. Furthermore, the modified specimens also display significantly lower power losses tested with a maximum magnetic flux density of 0.2 T at 50 Hz (0.076 ± 0.001 W kg⁻¹) and 100 Hz (0.204 ± 0.003 W kg⁻¹) compared to those of the toroidal Fe_{93.3}Si_{6.7} (wt%) specimens produced by Goll et al. using PBF-L.^[9] Even now, at low frequencies between 50 Hz and 100 Hz, the modified specimens possess a stable maximum magnetic flux density of ≈ 0.902 T which already outperforms some commercial soft magnetic materials; e.g., soft ferrites show the saturation magnetic flux density values in the range of 0.103–0.546 T;^[19,33–36] the saturation magnetic flux density values of Fe–Ni-based molypermalloy are reported to be ≈ 0.7 T;^[19,37] and the saturation magnetic flux density values of Fe–Ni-based supermalloy are commonly in the range of 0.66–0.82 T.^[19,37,38]

To sum up, to gain a clear correlation between the tailored structures and the magnetic performance, the toroidal geometry (i.e., height: 6.3 mm, outer/inner diameter: 16.0 mm/9.6 mm) of different specimens was kept constant in this study. Toroidal cores with the similar geometry have wide applications as electromagnetic compatibility (EMC) filters and chokes in the current market. In addition, because of the specifically developed processing strategies, precise energy input and controllable processing procedures, the modified specimens with the tailored structure inspired by the theory of ferromagnetism show promising magnetic properties outperforming traditionally fabricated and PBF-L-produced soft magnetic materials. Despite the small size of the toroidal Fe_{93.5}Si_{6.5} (wt%) specimens fabricated in this work, the basic understanding of the mechanism to improve the magnetic properties and the know-how to fabricate toroidal specimens with desired structures using PBF-EB can be easily transferred in future research work to produce larger specimens.

During PBF-EB, no support structures were printed between the start plate and the Fe_{93.5}Si_{6.5} (wt%) specimens; i.e., the printed parts and the start plate were separated by thin sintered powder layers, so that the Fe_{93.5}Si_{6.5} (wt%) specimens were easily removable from the substrate after PBF-EB using sandblasting, indicating that it is achievable to fabricate the final Fe_{93.5}Si_{6.5}

(wt%) specimens within one single step by means of PBF-EB requiring no additional post-machining. All the as-built toroidal Fe_{93.5}Si_{6.5} (wt%) specimens exhibit a similar roughness of the lateral surface (R_a : ≈ 20 μ m, see Table S2 in supporting information) resulting from the layer-by-layer fabrication principle during PBF-EB. The dense top surface (Figure 4e) of the modified specimens is significantly smoother (R_a : ≈ 1 μ m, see Table S2 in supporting information).

As shown in Figure 1a, the desired outer and inner diameter of the toroidal Fe_{93.5}Si_{6.5} (wt%) specimens should be 16.0 mm and 9.6 mm, respectively; while the default height should be 6.3 mm. All PBF-EB-produced Fe_{93.5}Si_{6.5} (wt%) specimens exhibit a higher outer diameter and a lower inner diameter compared to the default values (Table S1 in supporting information), which could be explained by the contour-melting prior to hatching, resulting in an over-dimensioned boundary area in the xx - and yy -directions. Nevertheless, the dimensional deviation from the desired values is highly reproducible for all specimens produced using different hatching strategies (Table S1 in supporting information). To minimize the dimensional inaccuracy, contour offset can be used for PBF-EB, which, however, is not the fundamental research goal of this study. Compared to the relatively low dimensional accuracy in the xx - and yy -directions, the height of the PBF-EB-fabricated specimens only shows a slight deviation from the default values (Table S1 in supporting information), which might originate from the presence of the slightly sintered Fe_{93.5}Si_{6.5} (wt%) powder particles within the specimens.

4. Conclusion

Owing to the high design freedom, high processing temperature and intrinsic in situ heat treatment, electron beam powder bed fusion (PBF-EB) is a highly promising technique to produce brittle Fe_{93.5}Si_{6.5} (wt%) soft magnetic materials with adapted structure. Above all, two hatching strategies (i.e., “radial hatching” and “circle hatching”) were applied to fabricate toroidal Fe_{93.5}Si_{6.5} (wt%) specimens. The circle-hatching specimens possess large relative permeability and small coercivity resulting in high maximum magnetic flux density, low hysteresis losses and therefore low power losses. This is due to the perfect match between the circular pattern resulting from the circle-hatching strategy and the pathway for magnetic field lines in the shape of

the enclosed circles, which indicates the easier (de)magnetization process. Based on these results, the circle-hatching strategy was further used to produce the modified Fe_{93.5}Si_{6.5} (wt%) specimens with a specific layered structure (i.e., “one dense layer + powder layers”). Because the dense layers provide a fully merged pathway that improves magnetic induction and smooth (de)magnetization, higher maximum magnetic flux density and lower hysteresis losses were obtained. At the same time, the insert of loose powder particles between the dense layers leads to high electrical resistance and thereby low eddy current losses of the modified specimens. It is worth mentioning that the modified specimens show higher maximum magnetic flux density and lower power losses at sub-kHz, outcompeting several soft magnetic materials fabricated by conventional techniques and laser powder bed fusion (LPBF).

Supporting Information

Supporting Information is available from the Wiley Online Library or from the author.

Acknowledgements

This work is financially supported by China Scholarship Council (CSC), and the authors gratefully acknowledge their colleagues at the University of Erlangen-Nuremberg for their help with this research, including Dr. Daniel Kübrich assisting with the magnetic tests, Mr. Nick Semyatov helping with the maintenance of Freemelt ONE machine, Mr. Jihui Ye aiding with the preheating step and post-heat-treatment, Mr. Johannes Bäreis assisting with the measurement of surface roughness, Ms. Larissa Wahl aiding with the XRD test, and Ms. Maria Schröder helping with the EBSD measurement.

Open access funding enabled and organized by Projekt DEAL.

Conflict of Interest

The authors declare no conflict of interest.

Data Availability Statement

The data that support the findings of this study are available from the corresponding author upon reasonable request.

Keywords

electron beam powder bed fusion (EB-PBF), Fe_{93.5}Si_{6.5} (wt%) soft magnetic materials, magnetic performance, novel hatching strategies, structure design

Received: January 27, 2023

Revised: April 5, 2023

Published online:

- [1] G. Ouyang, X. Chen, Y. Liang, C. Macziewski, J. Cui, *J. Magn. Magn. Mater.* **2019**, 481, 234.
[2] S. Chikazumi, C. D. Graham, *Physics of Ferromagnetism 2e*, Oxford University Press, Oxford, UK **2009**.

- [3] J. Yang, Z. Fu, J. Ye, D. Kübrich, C. Körner, *Scr. Mater.* **2022**, 210, 114460.
[4] O. Ikeda, Y. Himuro, I. Ohnuma, R. Kainuma, K. Ishida, *J. Alloys Compd.* **1998**, 268, 130.
[5] U. C. Özöğüt, A. Çakır, *J. Alloys Compd.* **2017**, 705, 126.
[6] W.-W. Zhang, H.-H. Xu, J.-L. Liang, W. Xiong, Y. Du, *J. Alloys Compd.* **2009**, 481, 509.
[7] A. Krings, A. Boglietti, A. Cavignino, S. Sprague, *IEEE Trans. Ind. Electron.* **2016**, 64, 2405.
[8] G. Ouyang, B. Jensen, W. Tang, J. Schlagel, B. Hilliard, C. Pan, B. Cui, K. Dennis, D. Jiles, T. Monson, *Acta Mater.* **2020**, 201, 209.
[9] D. Goll, D. Schuller, G. Martinek, T. Kunert, J. Schurr, C. Sinz, T. Schubert, T. Bernthaler, H. Riegel, G. Schneider, *Addit. Manuf.* **2019**, 27, 428.
[10] R. Hilzinger, W. Rodewald, *Magnetic Materials: Fundamentals, Properties and Applications*, Vacuumschmelze, Hanau, Germany, **2013**.
[11] A. Aharoni, *Introduction to the Theory of Ferromagnetism*, Clarendon Press, Oxford, UK **2000**.
[12] Y. Liang, S. Wang, H. Li, Y. Jiang, F. Ye, J. Lin, *Adv. Mater. Sci. Eng.* **2015**, 2015, 296197.
[13] S. Wang, Y. Jiang, Y. Liang, F. Ye, J. Lin, *Adv. Mater. Sci. Eng.* **2015**, 2015.
[14] O. Fischer, J. Schneider, *J. Magn. Magn. Mater.* **2003**, 254, 302.
[15] F. Fiorillo, *Characterization and Measurement of Magnetic Materials*, Academic Press/Elsevier, **2004**.
[16] H. Shimanaka, Y. Ito, K. Matsumara, B. Fukuda, *J. Magn. Magn. Mater.* **1982**, 26, 57.
[17] T. Kan, Y. Ito, H. Shimanaka, *J. Magn. Magn. Mater.* **1982**, 26, 127.
[18] Z. Fu, C. Körner, *Euro. J. Mater.* **2022**, 2, 54.
[19] T. N. Lamichhane, L. Sethuraman, A. Dalagan, H. Wang, J. Keller, M. P. Paranthaman, *Mater. Today Phys.* **2020**, 15, 100255.
[20] C. Korner, *Int. Mater. Rev.* **2016**, 61, 361.
[21] J. A. Koepf, M. R. Gotterbarm, M. Markl, C. Körner, *Acta Mater.* **2018**, 152, 119.
[22] B. Vayre, F. Vignat, F. Villeneuve, *Mech. Ind.* **2012**, 13, 89.
[23] K. V. Wong, A. Hernandez, *Int. Scholarly Res. Not.* **2012**, 2012.
[24] F. Fiorillo, G. Bertotti, C. Appino, M. Pasquale, in: *Wiley Encyclopedia of Electrical and Electronics Engineering*, John Wiley & Sons, Inc., **2016**, pp. 1–42.
[25] C.-W. Chen, *Magnetism and Metallurgy of Soft Magnetic Materials*, Courier Corporation, **2013**.
[26] B. D. Cullity, C. D. Graham, *Introduction to Magnetic Materials*, John Wiley & Sons, Hoboken, NJ, USA **2011**.
[27] J. Dubowik, *Phys. Rev. B* **1996**, 54, 1088.
[28] M. Grimsditch, Y. Jaccard, I. K. Schuller, *Phys. Rev. B* **1998**, 58, 11539.
[29] D.-X. Chen, E. Pardo, A. Sanchez, *IEEE Trans. Magn.* **2005**, 41, 2077.
[30] G. Wysin, "Demagnetization Fields", <https://www.phys.ksu.edu/personal/wysin/notes/demag.pdf>, **2012**.
[31] D. Zhang, *J. Magn. Magn. Mater.* **2000**, 221, 414.
[32] T. Li, Y. Wang, H. Shi, L. Xi, D. Xue, *J. Magn. Magn. Mater.* **2022**, 545, 168750.
[33] K. Jalaiah, K. C. Mouli, R. Krishnaiah, K. V. Babu, P. S. Rao, *Heliyon* **2019**, 5, e01800.
[34] C. Ding, L. Liu, Y. Mei, K. D. Ngo, G.-Q. Lu, in *2018 IEEE Applied Power Electronics Conf. and Exposition (APEC)*, IEEE, Piscataway, NJ, USA **2018**, pp. 615–618.
[35] L. Liu, T. Ge, K. D. Ngo, Y. Mei, G.-Q. Lu, *IEEE Magn. Lett.* **2018**, 9, 5102705.
[36] I. Gul, A. Abbasi, F. Amin, M. Anis-ur-Rehman, A. Maqsood, *J. Magn. Magn. Mater.* **2007**, 317, 494.
[37] I. Chichinas, V. Pop, O. Isnard, *J. Mater. Sci.* **2004**, 39, 5305.
[38] S. A. Firdosy, N. E. Ury, R. Witt, R. P. Dillon, V. A. Ravi, *Metallogr., Microstruct., Anal.* **2022**, 11, 108.